

USGS National Earthquake Hazards Reduction Program

Final Technical Report

Evaluation and Application of LiDAR data to constraining a late Pleistocene slip rate and vertical deformation of the Northern San Andreas Fault, Fort Ross to Mendocino, California: Collaborative research between Arizona State University and the U.S. Geological Survey

USGS NEHRP # 06HQGR0032

Principal Investigator J Ramón Arrowsmith
Chris Crosby
School of Earth and Space Exploration
Arizona State University
Tempe, AZ 85287-1404
Office: (480) 965-3541
Fax: (480) 965-8102
ramon.arrowsmith@asu.edu

Summary

The purpose of this study was two-fold: (1) Evaluate LiDAR data as a tool for studying tectonic geomorphology and earthquake geology and develop methodologies for utilizing these types of data in determining various geomorphic metrics of surface processes and landscape history. (2) Characterize the tectonic geomorphology of the NSAF at various temporal and spatial scales in order to better understand San Andreas fault geometry, slip distribution and off-fault deformation as manifest in landscape development and response.

Table of contents

Summary 1

Introduction 2

Evaluate LiDAR data as a tool for studying tectonic geomorphology and earthquake geology 3

 GEON LiDAR Workflow and science community support 3

 Exploiting LiDAR for Regional Morphologic Correlation and Dating of Wave-cut and Fault-Controlled Landforms 4

Exploration of LiDAR point cloud data artifacts, return density, and digital elevation model generation ... 13

Characterize the tectonic geomorphology of the NSAF at various temporal and spatial scales in order to better understand San Andreas fault geometry, slip distribution and off-fault deformation as manifest in landscape development and response. 24

Presentations and Publications 28

References 29

Introduction

The objective of this research was to analyze LiDAR (LIght DIstance And Ranging) topographic data of the Gualala block section of the northern San Andreas fault (NSAF) and associated marine terraces between the towns of Fort Ross and Mendocino, California acquired in February of 2003 to gain earthquake hazard understanding for the NSAF (Figure 1). The purpose was twofold: (1) Evaluate LiDAR data as a tool for studying tectonic geomorphology and earthquake geology and develop methodologies for utilizing these types of data in determining various geomorphic metrics of surface processes and landscape history. (2) Characterize the tectonic geomorphology of the NSAF at various temporal and spatial scales in order to better understand San Andreas fault geometry, slip distribution and off-fault deformation as manifest in landscape development and response.

Specifically, we are focused on the late Pleistocene marine terraces in this region and their importance in constraining a SAF slip rate at Alder Creek, near Point Arena, where the terraces are offset by the fault as it intersects the coast.

In addition, we analyzed the topography along the NSAF to constrain patterns of distributed, SAF-driven, deformation recorded in the landscape. Such patterns of deformation may reflect SAF geometry and may be useful for inferring rupture behavior and slip history.



Figure 1. Map showing extent of NSAF LiDAR coverage and proposed study area. NSAF data is represented as a hillshade image. Trace of the 1906 earthquake rupture is shown in red. (Jennings, 1994). "Example 3" box shows approximate location of Figure 2. Figure taken directly from: <http://quake.usgs.gov/research/geology/lidar/> without modification.

Evaluate LiDAR data as a tool for studying tectonic geomorphology and earthquake geology

GEON LiDAR Workflow and science community support

Digital data acquisition technologies such as LiDAR (Light Distance And Ranging) topography have resulted in an increase in the volume and complexity of scientific data that must be efficiently managed, distributed and processed in order for it to be of use to the scientific community. Capable of generating digital elevation models (DEMs) more than an order of magnitude more accurate than those currently available, LiDAR data offers the opportunity to study earth surface processes at resolutions not previously possible yet essential for their appropriate representation.

Unfortunately, access to these datasets for the average user is difficult because of the massive volumes of data generated by LiDAR. The distribution and processing of large LiDAR datasets, which frequently exceed billions of data-points, challenge internet-based data distribution systems and readily available desktop software. Figure 1 shows the conceptual workflow required to produce results for scientific analysis using LiDAR.

Our approach to the distribution and processing of LiDAR data capitalizes on cyberinfrastructure developed by the GEON project (<http://www.geongrid.org>) to harness distributed computing resources. We utilize a workflow-based solution, the GEON LiDAR Workflow (GLW), which begins with user-defined selection of a subset of point data and ends with download (including dynamically generated metadata) and visualization of DEMs and derived products. Users perform point cloud data selection, interactive DEM generation and analysis, and visualization all from an internet-based portal. Users may experiment with DEM resolution and DEM generation algorithms so as to optimize terrain models for their application. By using cyberinfrastructure resources, this approach allows users to carry out computationally intensive LiDAR data processing without having appropriate resources locally.

In this project, we coordinated with our GEON colleagues to serve the Northern California earthquake science community by providing training and assistance on access to and processing of Northern San Andreas Fault LiDAR data (NASA/USGS). As of April 23, 2008, 972 NSAF jobs were submitted processing of 6,610,365,763 points. Our contributions included numerous informal consultations with colleagues about the LiDAR data and processing of it. In addition, we contributed significant images and expertise to the Northern California LiDAR workshop led by Kevin Furlong. Figure 2 shows an example of the tectonic geomorphology along the San Andreas Fault near Mill Gulch south of Point Arena.

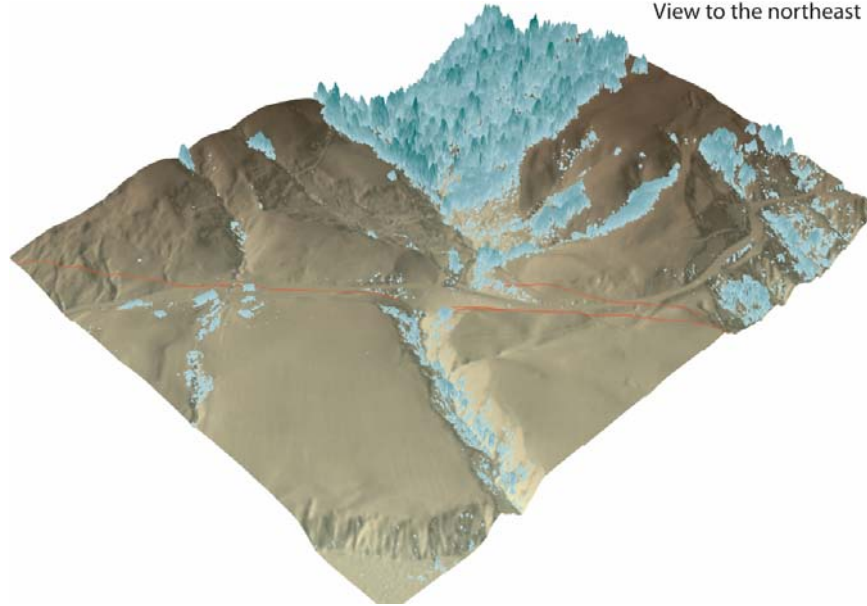


Figure 2. Example view of gridded LiDAR data selected and processed in the GLW using the NASA/USGS dataset for the Northern San Andreas Fault. In this ~2 m digital elevation model of Mill Gulch, the green areas show the vegetative canopy taller than about 50 cm overlain on the topography. Canopy height is colored in shades of green with darker colors indicating taller trees. The red lines show the discontinuous traces of the San Andreas Fault which broke in the 1906 earthquake.

Exploiting LiDAR for Regional Morphologic Correlation and Dating of Wave-cut and Fault-Controlled Landforms

The capability to generate high-resolution Digital Elevation Models (DEMs) from LiDAR data (Light Distance and Ranging, also known as Airborne Laser Swath Mapping, or ALSM) across broad geographic regions provides a new tool for studying landscape response to tectonic deformation. Expanded LiDAR coverage from the Plate Boundary Observatory (PBO) and the National Center for Airborne Laser Mapping (NCALM) offers the prospect of applying these data to a variety of tectonic geomorphic studies. The data volume and point-density of LiDAR allows extensive repetition of profile-based landscape analyses without the need for laborious total station transects. Traditional DEMs, such as the USGS National Elevation Dataset, lack the resolution necessary for these types of analyses.

We exploited LiDAR data for landform correlation by conducting profile-based morphologic dating (linear and non-linear diffusion) of fault scarps and marine, lake and fluvial shorelines. In brief, this method assumes that topographic profile development ($H(x,t)$) results solely from transport limited erosion and deposition of slope dependent hillslope transport (e.g., Hanks, et al., 1984; Hanks, 2000):

$$H(x, t) = (\theta - b) \left(\frac{\kappa t}{\pi} \right)^{1/2} \left\{ \exp \left(- \frac{x + a/(\theta - b)}{4\kappa t} \right)^2 - \exp \left(- \frac{x - a/(\theta - b)}{4\kappa t} \right)^2 \right\} \\ + \frac{\theta - b}{2} \left\{ \left(x + \frac{a}{\theta - b} \right) \operatorname{erf} \left(\frac{x + a/(\theta - b)}{(4\kappa t)^{1/2}} \right) - \left(x - \frac{a}{\theta - b} \right) \operatorname{erf} \left(\frac{x - a/(\theta - b)}{(4\kappa t)^{1/2}} \right) \right\} \\ + bx$$

θ is initial scarp slope, b is the far-field or fan slope, k is the transport rate, t is time (note that kt is the morphologic age—the unique measure of scarp form with respect to age and transport rate. It has dimensions of m^2). Figure 3 shows the evolution of a simple scarp.

The resolution and geographic extent of LiDAR coverage makes broad spatial correlations possible, assuming that controls on the hillslope processes are relatively constant across the region. Due to the high data density, numerous topographic profiles can be extracted from a DEM and analyzed for morphologic age. Correlation from profile to profile can then be established by comparing morphologic age for various landforms in a research area. With calibration, morphologic dating also offers the opportunity to constrain absolute ages of landforms. Once calibrated, landforms across the region can be quickly dated via profile-based analysis of the LiDAR-derived DEM. In addition, morphologic comparison of landforms of known age offers the opportunity to test the role of other constraints, such as aspect, microclimate, and substrate type on landform development by diffusive processes.

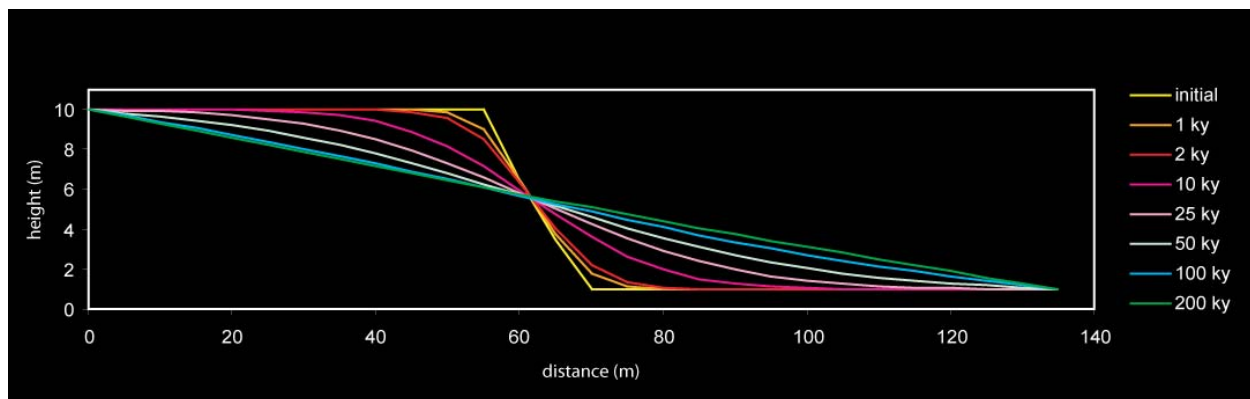


Figure 3. Model of simple linear diffusion of a theoretical scarp-like landform. Our algorithm assumes initially vertical riser morphology rapidly evolves to a steep, ramp-shaped topography via mass wasting processes immediately after formation. Diffusive process then continue to modify the riser (e.g. Rosenbloom and Anderson, 1994; Hanks et al., 1984, Hanks, 2000).

Tests on synthetic profiles demonstrate the ability of morphologic dating to differentiate landforms of morphologic age 50 m^2 from ones of 100 m^2 . Figure 3 shows the results of the analysis. We used the *Diffusion scarp dater* written by George Hilley (Hilley, 2001 and Hilley and Arrowsmith, 2001). It allows calculation of finite scarp Root Mean Square Error for fits of observed (LiDAR-derived) profile compared to modeled profile and forward modeling of topographic transect data. It is available at: <http://activetectonics.asu.edu/diffuse>. We were certainly able to differentiate the two different-aged landforms, even accounting for ± 50 cm of noise in the profiles.

To continue the evaluation of the method, we revisited the classic diffusion modeling studies of Hanks, et al., 1984 of the Santa Cruz, California sea cliffs (figure 5 and table 1) and the Hanks and Wallace, 1984 study of the Lake Lahontan shoreline scarps (figure 6 and table 2). The results show that indeed we could replicate their results, but the method is not strongly sensitive to varying parameters, so our equally good results for the Santa Cruz shoreline differs by several hundred m^2 which is tens of kyr.

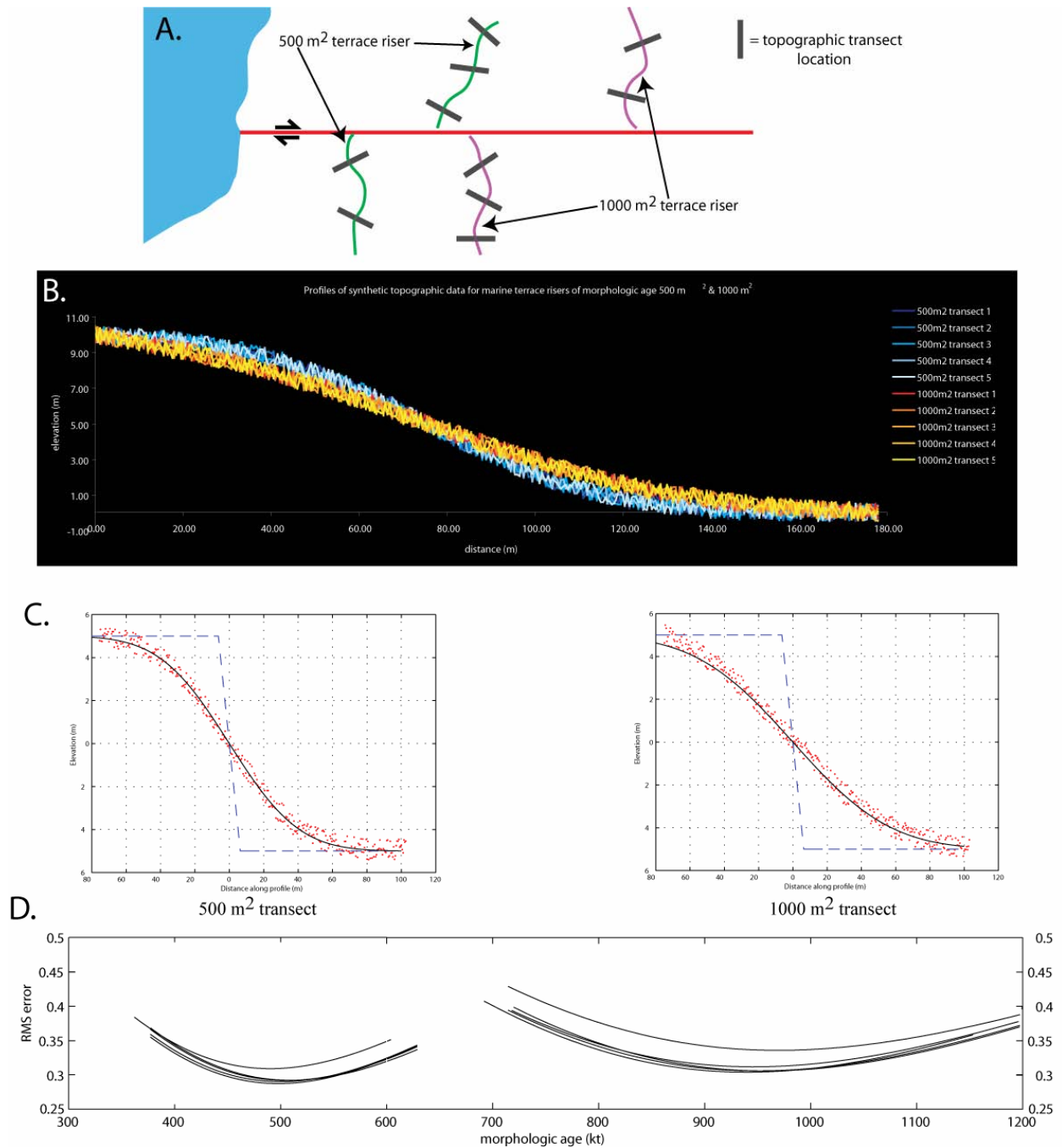


Figure 4. Illustration of morphologic dating approach that we exploited. In this contrived example, 5 profiles each from the two terrace risers shown in map view in A are analyzed. B) The synthetic profiles were produced by forward model calculations of 500 and 1000 m² profiles starting with a 10 m riser and flat tread (for a diffusion constant (k) of 10 m²/ka the morphologic age (kt) yields an absolute age of 50,000 yrs and 100,000 yrs respectively). To the resulting profiles we added +/- 50 cm of noise to simulate local heterogeneity in the surface as is typically encountered and would be likely in the LiDAR derived profiles. Profile data shown in shades of blue are 500 m² risers while red and yellow data are from 1000 m² risers C) Best fitting model profiles to the synthetic "data." D) Illustration of the relationship between RMS and morphologic age for the 5 different profiles of the two different risers.

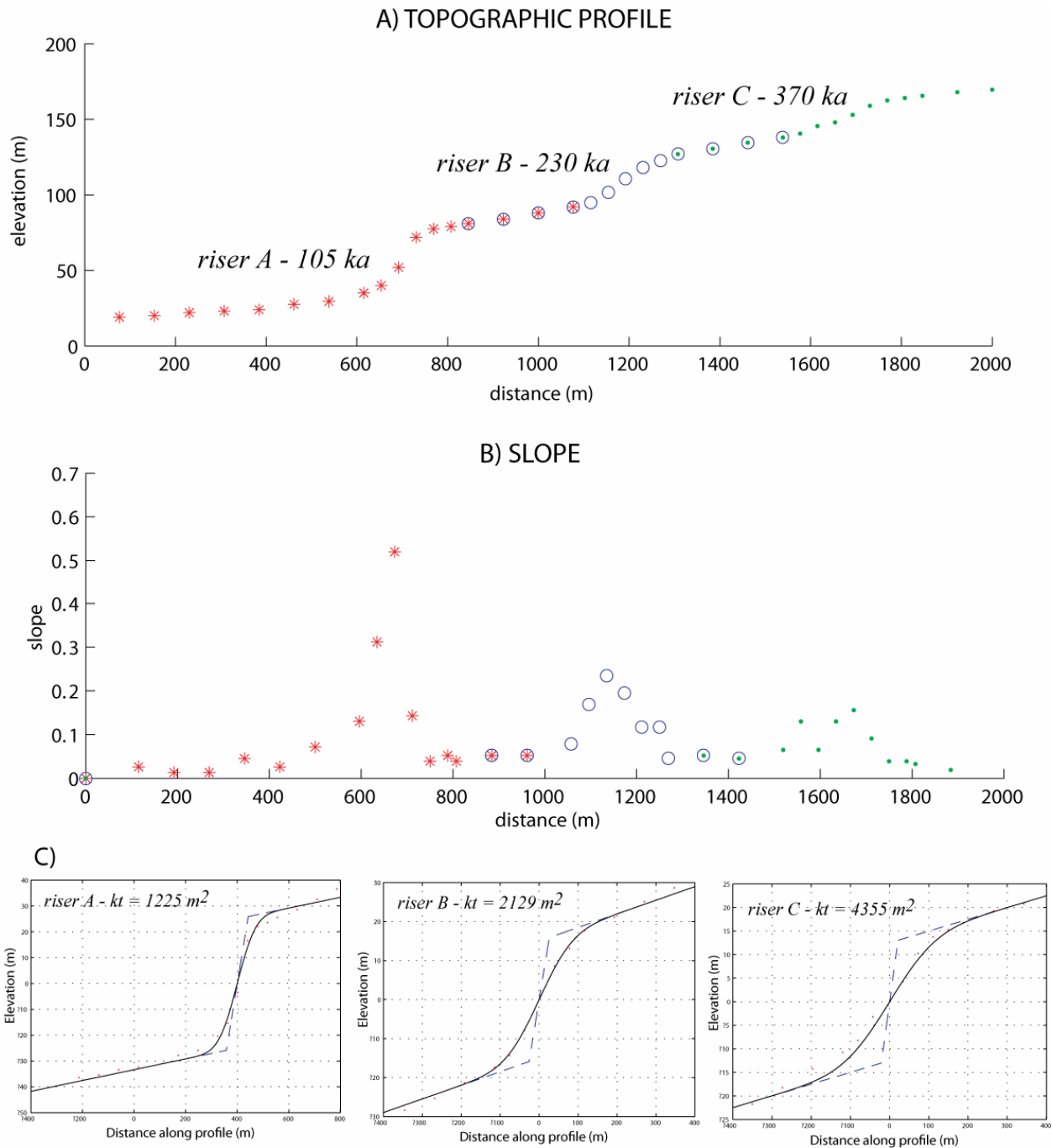


Figure 5. A) Santa Cruz, CA marine terrace topographic profile recreated from Hanks et al., 1984. Ages for the three risers come from U-Th and amino acid racemization data, global sea level curves and the assumption of a constant uplift rate of 0.35 m/ka (see Hanks et al., 1984 B) Plot showing slope calculated along the marine terrace topographic profile. Plot illustrates qualitative observation that the older risers have more subtle topography - peak slope diminishes and the scarp widens. C) Model calculations (solid lines) for the Santa Cruz terrace risers. Assumed initial morphology shown as dashed blue line. Actual topography shown as red dots. Model parameters are summarized in table 1.

Table 1. PARAMETERS / RESULTS

k for Santa Cruz terraces:
11 m²/ka

Hanks et al., 1984

Sea Cliff	2a (m)	age (ka)	b (upper)	b (lower)	kt (m ²)
A	50	105	0.04	0.02	1200
B	30	230	0.05	0.02	2500
C	31	370	0.03	0.02	4100

This study

Sea Cliff	2a (m)	age (ka)	b (setup)	b (calculated)	kt (m ²)	theta
A	50	105	0.03	0.021	1226	35
B	30	230	0.035	0.035	2129	35
C	31	370	0.025	0.021	4355	35

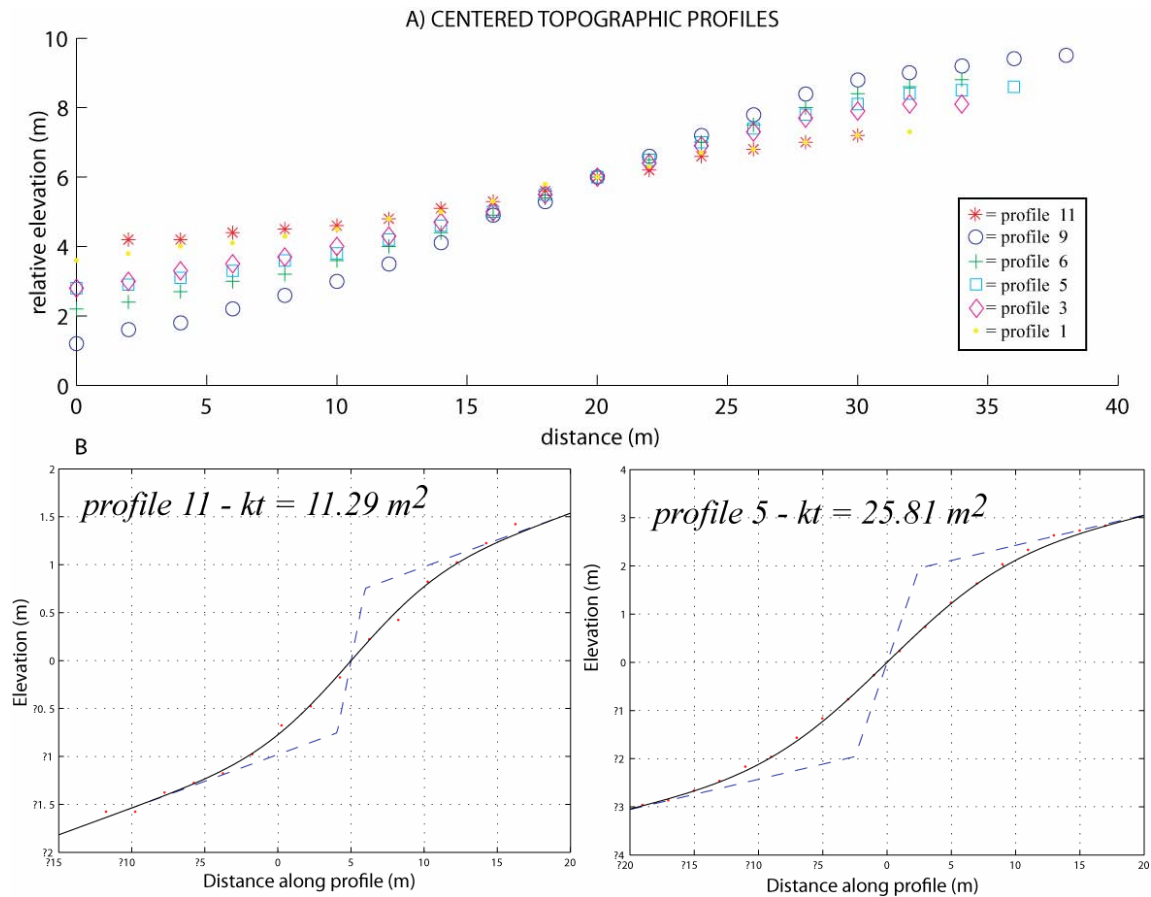


Figure 6. A) Lake Lahontan shoreline topographic profiles recreated from Hanks & Wallace, 1985. Shown are the profiles for which Hanks & Wallace performed model calculations. B) Model calculations (solid lines) for two Lake Lahontan shorelines. Assumed initial morphology shown as dashed blue line. Actual topography shown as red dots. Model parameters are summarized in Table 2.

Table 2. PARAMETERS / RESULTS

k for Basin and Range: 1.1 m²/ka

Hanks & Wallace, 1985

This study

profile #	a	b (deg.)	kt (m ²)	profile #	a	b (setup)	b (calculated)	kt (m ²)	theta
11	0.7	3.5	16	11	0.7	3.5	3.2	11.29	45
9	2.5	3.5	25	9	2.5	3.5	4	20.97	45
6	2	3.5	25	6	2	3.5	4	25.81	45
5	1.8	3.5	25	5	1.8	3.5	3.6	25.81	45
3	1.6	3.5	25	3	1.6	3.5	3.6	25.81	45
1	0.7	3.5	16	1	0.7	3.5	4	14.52	45

Application of this technique to recently acquired LiDAR datasets in northern California and in the Basin and Range province illustrates the power of morphologic dating for establishing correlations among regional landforms.

We blindly applied the morphologic dating technique discussed above to fault scarps cutting the Sheep Creek alluvial fan in Death Valley California (thanks to Thad Wasklewicz, U. Memphis, for generously sharing a portion of his Death Valley ALSM dataset). Topographic profiles were extracted from the ALSM data and then analyzed for morphologic age (Table 3). Figure 7 shows the map location of the profiles on shaded relief and a simple slope offset analysis (evaluates the changing slope at the scarp midpoint as a function of the offset and age). Plotting the topographic transects in the slope offset space revealed significant variation in κt along strike. The slope offset plot suggests low morphologic ages ($< 5 \text{ m}^2/\text{ka}$) for the Sheep Creek scarps. It is difficult to assign any scarp to a single κt . Many of the topographic profiles reveal an over-steepening of the scarp near its base and a bevel in the upper scarp. Qualitative forward modeling of these transects may yield a very different κt than that of the analytical solution, depending upon what portion of the scarp one chooses to fit.

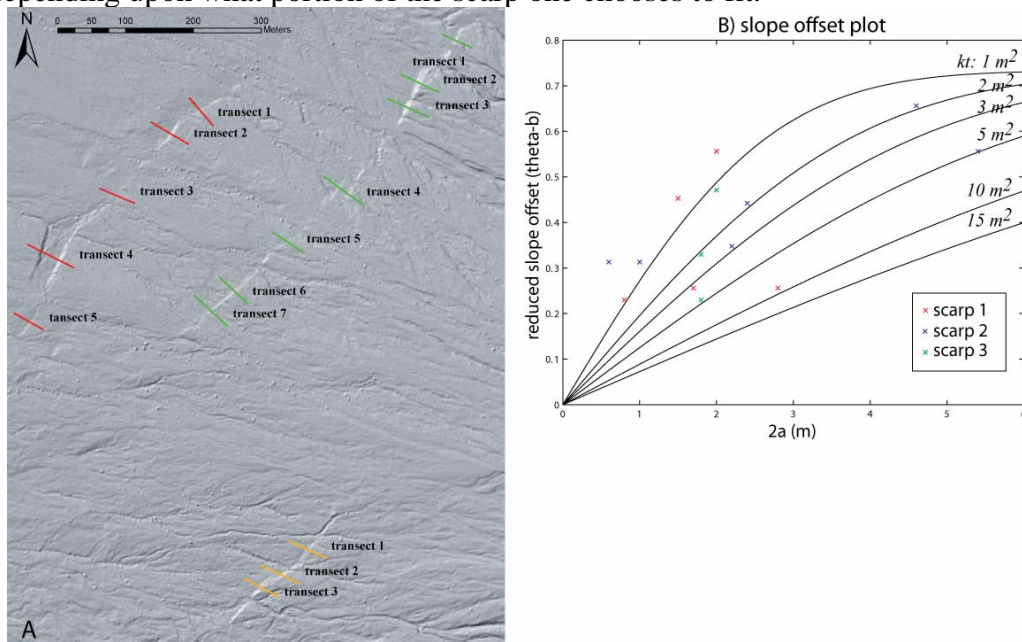


Figure 7. A) Hillshade of 1 m DEM derived from ALSM data. Three fault scarps clearly offset the Sheep Creek fan. Locations of topographic profiles extracted from the DEM are shown as colored lines (red: scarp 1, green: scarp 2, orange: scarp 3). B) Slope offset plot for topographic transects across the three Sheep Creek fan scarps. Transect data shown as colored Xs. Also shown are model calculations for a variety of κt values. The transects generally plot at low κt values ($< 5 \text{ m}^2/\text{ka}$) however the significant scatter in the data makes it difficult to associate any scarp with a single κt value.

Table 3. PARAMETERS / RESULTS Sheep Creek

Scarp 1

transect #	a (m)	b (setup)	b (calculated)	kt (m ²)	
				qualitative	calculated
1	0.85	2.5	2	5 - 21	9.68
2	1	2.5	2.4	1	1.61
3	0.75	2.7	2.8	15	17.74
4	1.4	2.5	0.8	2 - 15	4.84
5	0.4	4	3.2	0.3 - 2	-

Scarp 2

transect #	a (m)	b (setup)	b (calculated)	kt (m ²)	
				qualitative	calculated
1	1.2	3.3	3.2	2 - 15	48.39
2	2.7	2.5	2.4	10 - 60	25.81
3	2.3	2.5	2	1	16.13
5	0.3	5	-	1	-
6	0.5	5	4	0.3	-
7	1.1	3	2.8	7	32.26

Scarp 3

transect #	a (m)	b (setup)	b (calculated)	kt (m ²)	
				qualitative	calculated
1	0.9	4	4	3 - 15	19.35
2	1	4.5	4	2	9.68
3	0.9	4	3.6	2	9.68

Morphologic dating has potential utility for correlating marine terraces over significant lengths of coast line. In this final portion of the morphologic dating study, we compared topographic transects extracted from a small piece of coastal LiDAR data to test the technique's ability to differentiate risers of different ages. We applied this to the extensive marine terraces mapped by Prentice and Crosby at Point Arena (Figures 8, 9, and Table 4).

Table 4. PARAMETERS / RESULTS for Pt. Arena terraces

RISER 1 - stage 5a (~83 ka)

transect #	a (ft)	b (setup)	b (calculated)	qualitative	calculated	k (m ² /ka)	theta	
				kt (m ²)	kt (m ²)			
1	27	1.5	1.6	2300	3710	27.71	35	excess mass
2	22.5	1.6	1.6	3500	5161	42.17	35	excess mass
3	14.5	2	2	2742	2742	33.04	35	
4	15	2	2	3500	7742	42.17	35	excess mass
5	24	1.5	1.6	2000	3226	24.10	35	

RISER 3 - stage 7 (~194 ka)

transect #	a (ft)	b (setup)	b (calculated)	qualitative	calculated	k (m ² /ka)	theta	
				kt (m ²)	kt (m ²)			
1	24	1.8	1.6	10323	10323	53.21	35	
2	29	2.5	2.4	6000	9032	30.93	35	excess mass
3	23	5	-	1000	-	5.15	35	rejuvenated
4	26.5	2	2	600	645	3.09	35	rejuvenated
6	31	2.5	2.4	1500	2581	7.73	35	rejuvenated
7	17	3	3.2	7742	7742	39.91	35	
8	27	2	1.2	871	871	4.49	35	rejuvenated

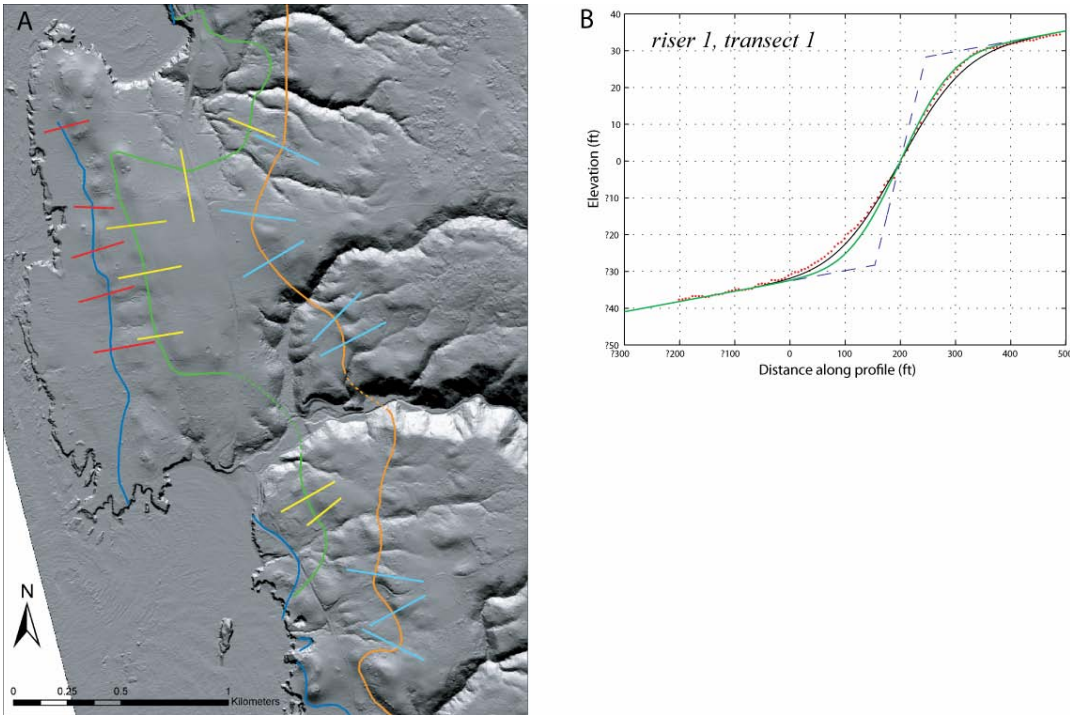


Figure 8. A) Hillshade of 1.8 m bare earth DEM derived from LiDAR data. The three lowest marine terrace risers are mapped by colored lines (blue: riser 1, green: riser 2, orange: riser 3). Mapping is from aerial photography and the LiDAR data. Topographic profiles extracted for this study are shown as straight line segments, colored by riser. B) Calculated model fit to transect across riser 1 (black line). The green line shows a qualitative best fit to the upper portion of the riser. The analytical solution is driven to higher κt s due to excess mass on the terrace platform. We favor a best fitting model of the upper riser where the mass excess problem exists.

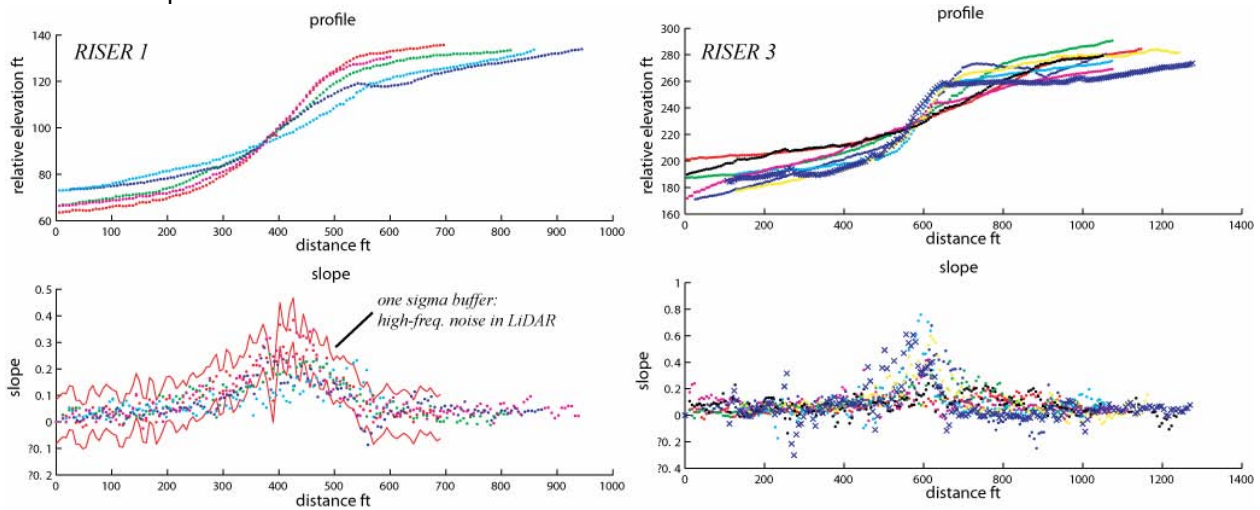


Figure 9. Riser 1. Upper plot shows centered topographic profiles across riser 1. Lower plot shows slope along the topographic profile. Red lines denote one sigma buffer around the red profile to demonstrate the extent of the high-frequency noise in the LiDAR data. Note the along strike variation in riser morphology. Riser 3. Upper plot shows centered topographic profiles across riser 3. Lower plot shows slope along the topographic profile. Note the along strike variation in riser morphology - risers shown with blue, yellow and cyan dots and blue x's all show evidence for rejuvenation.

In conclusion, application of morphologic dating techniques to LiDAR/ALSM datasets offers an opportunity to correlate landforms over broad geographic regions. This study demonstrates that diffusion equation analysis is an over-simplified technique that is highly dependent on transect selection. The abundance of high-resolution topographic data provided by LiDAR creates a new suite of complications that need to be addressed in order to make morphologic correlation effective. Ultimately, these complications provide insight into the geomorphic process. Complications in the morphologic age analysis can be traced to these causes: landform rejuvenation, non-transport limited conditions, non-linear diffusion, and non-diffusive conditions. High-frequency noise in the LiDAR data effects slopes along the profile. Undersampling or filtering the DEM for the slope calculations helps with this problem. Further statistical analysis of the profile data will quantify correlation and help to resolve some of the complications that LiDAR data introduces to morphologic analysis.

Exploration of LiDAR point cloud data artifacts, return density, and digital elevation model generation

The growing availability of LiDAR (Light Distance And Ranging (a.k.a. ALSM – Airborne Laser Swath Mapping)) data in the earthquake geology and tectonic geomorphology communities means that these powerful data are being utilized in an increasing number of research projects. LiDAR point cloud data (x, y, z, return classification) (Figure 10) are challenging to manipulate, so users typically only take advantage of interpolated surfaces (digital elevation models; DEMs) generated by the LiDAR data vendor for their analysis. However, by not returning to the LiDAR point cloud data, users may fail to fully exploit the richness of these data sets.

Initiating geomorphic analyses and visualizations with the point cloud gives users more understanding of the data and control over how those data characterize the landscape. Details such as the interpolation algorithm and grid resolution can significantly affect the manner in which the resulting DEM represents the landscape. In addition, beginning with the LiDAR point cloud data allows the user to assess the homogeneity and density of ground returns in the area of interest (Figure 11) and to evaluate potential artifacts in the data caused by errors in data acquisition and processing (e.g. point misclassification) (Figure 10). By understanding the variation in ground return density (which can vary due to topography, canopy characteristics and acquisition parameters) (Figure 11), the user has a better understanding of potential artifacts that may be introduced into their DEMs by this variation.

Using LiDAR point cloud data from the Northern San Andreas Fault (Figure 1) recently made available via the GEON LiDAR Workflow (GLW) (<http://www.geongrid.org/science/lidar.html>), we focused on evaluation of LiDAR point return density in both forested and unforested landscapes near Fort Ross, California. This prototypical methodology was originally presented as Crosby et al., 2006 and demonstrates that by evaluating LiDAR ground return density before generating a DEM, the user is able to performed “informed” DEM generation whereby the resolution of the DEM is optimized to take full advantage of the data resolution (Figures 11, 12, and 14). This analysis revealed that DEMs generated from LiDAR point cloud data often do not take full advantage of the point return density, producing DEMs that have multiple returns per DEM cell. LiDAR DEMs can be accurately produced down to a one point per pixel on average threshold. We also explore the accuracy of common DEM interpolation algorithms to fit the LiDAR point cloud (Figure 13). In areas of high-ground return density relative to the grid resolution, there is little variation between interpolation algorithms in the accuracy with which they fit LiDAR ground returns.

Through interactive exploration and interpolation of LiDAR point cloud data, users gain a better understanding of the strengths and weakness of their data and are able to optimize DEM generation to represent the landscape they are studying. This approach to working with LiDAR data allows tectonic landforms to be delineated more efficiently and with greater detail than by working with the vendor generated DEMs.

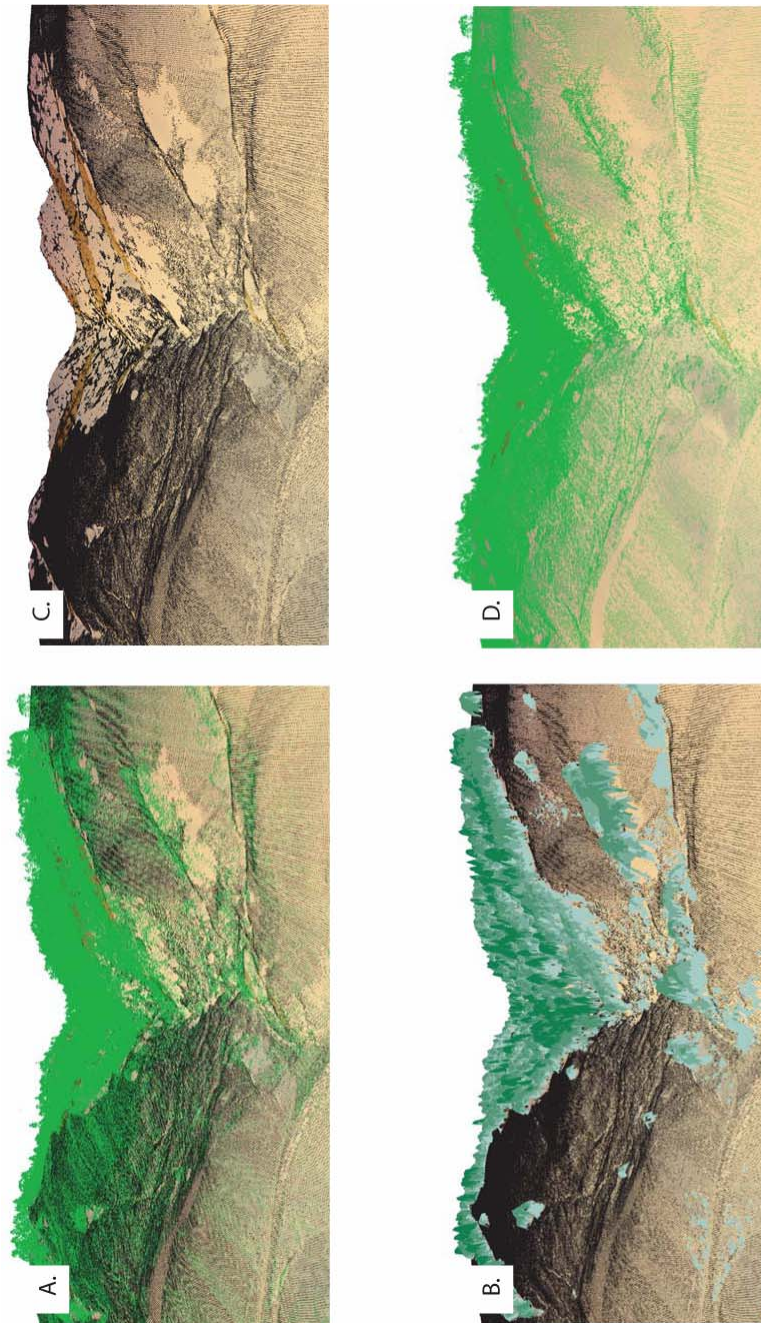
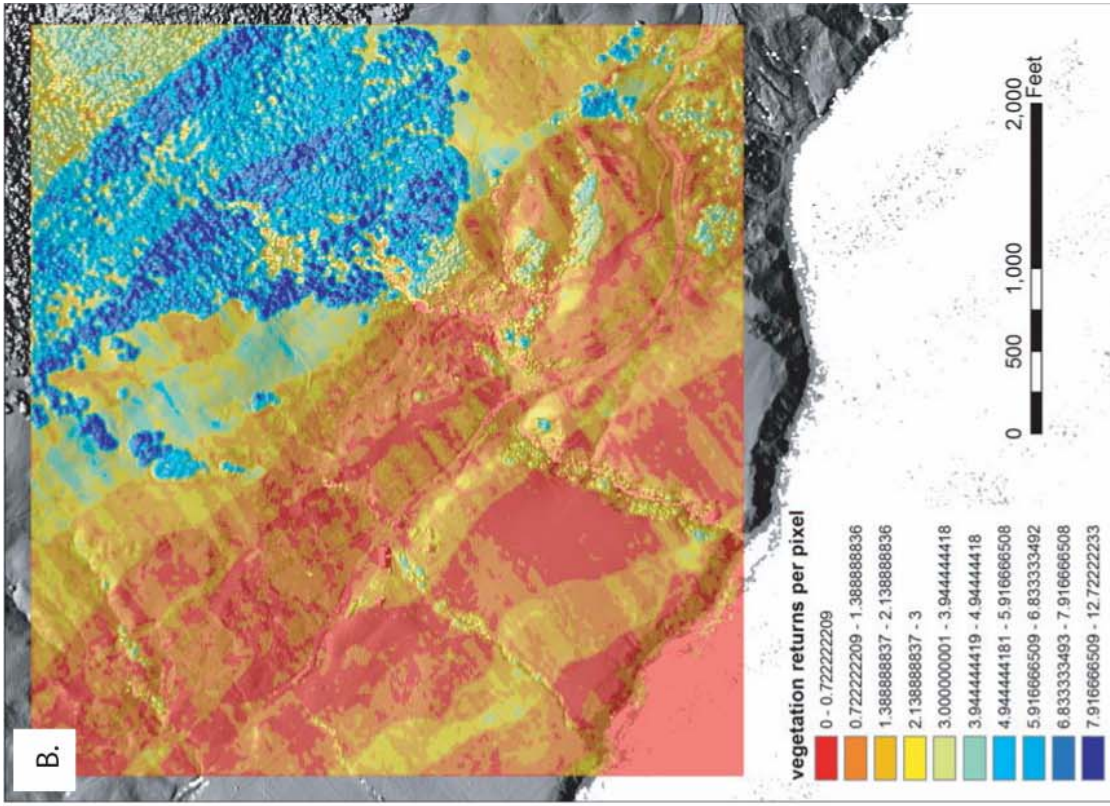
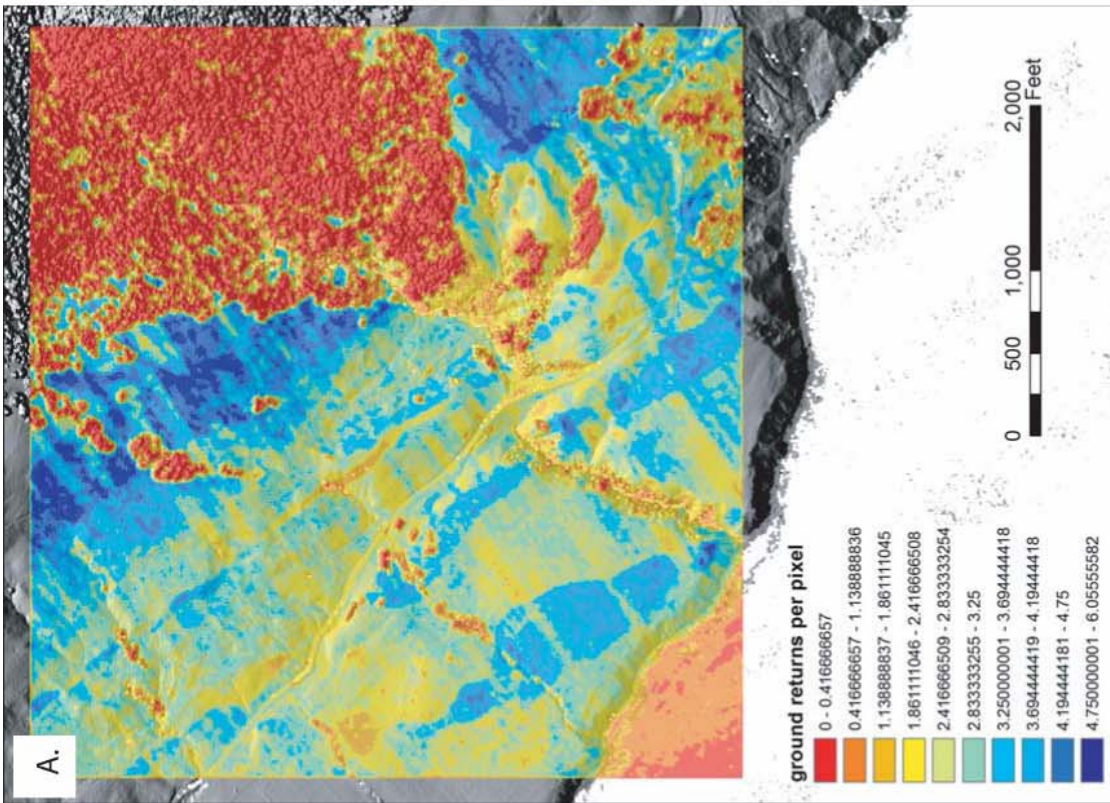


Figure 10. 3D visualization of classified LiDAR point cloud data. These images show a NE view up Mill Gulch near Fort Ross, CA. Note U.S. Highway One in the lower left of each image. A) 3D rendering of ground returns (black) and vegetation returns (green) over the bare earth DEM (brown). B) 3D rendering of ground returns (black) and vegetation DEM (shades of green color coded by height with darker shades of green for taller vegetation -- maximum tree height is approximate 280 ft) over the bare earth DEM (brown). C) 3D rendering of ground returns (black) over the bare earth DEM (brown). Note the lack of ground returns (gaps in the black points) underneath the canopy. D) 3D rendering of vegetation returns (green) over the bare earth DEM (brown). Note returns classified as vegetation on the flat surfaces in the foreground. These points are misclassified, reclassifying them as ground returns would yield higher ground return densities in these areas. The misclassification of these points is likely an error due to swath mismatches within the processed data set. This offset is likely traceable to the mislocation of the aircraft due to GPS or Inertial Navigation problems.



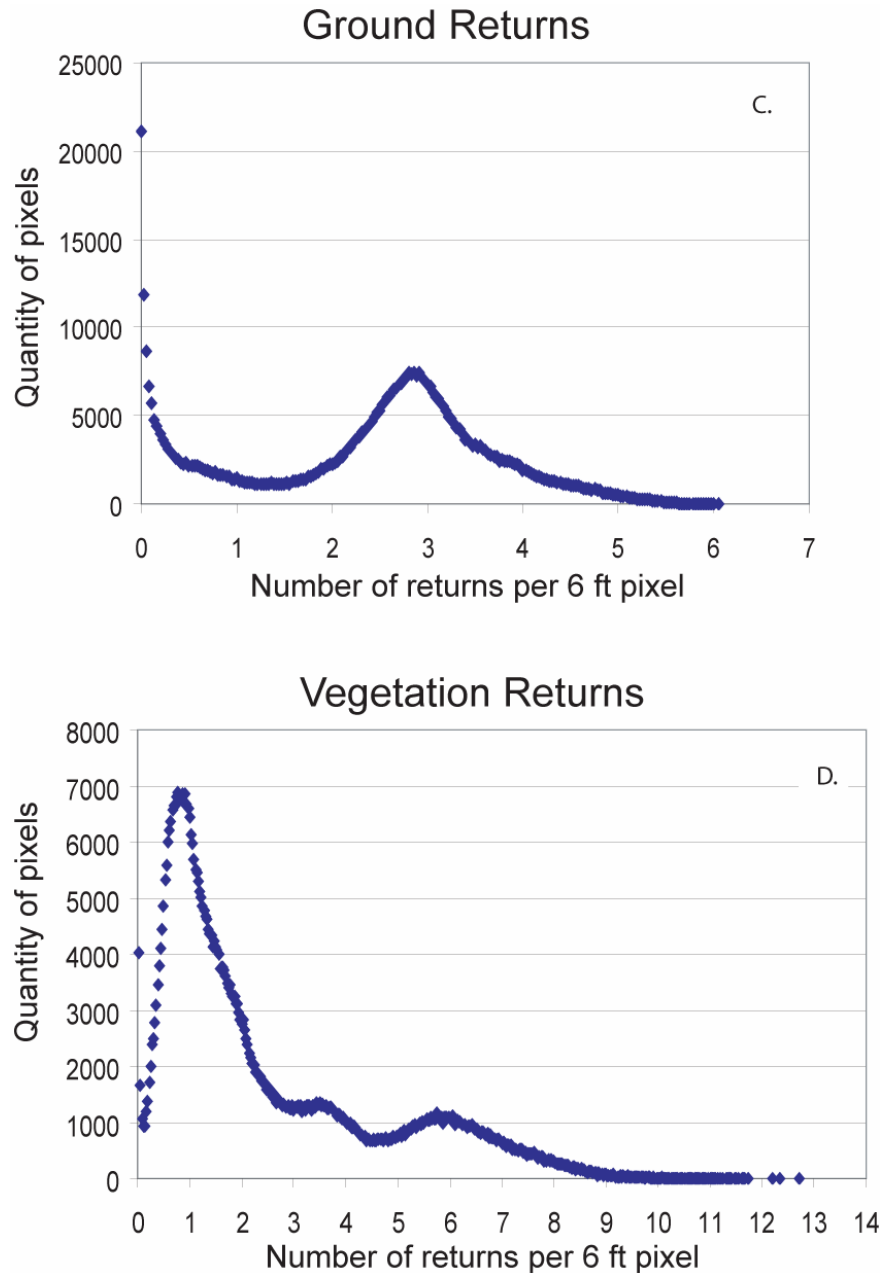
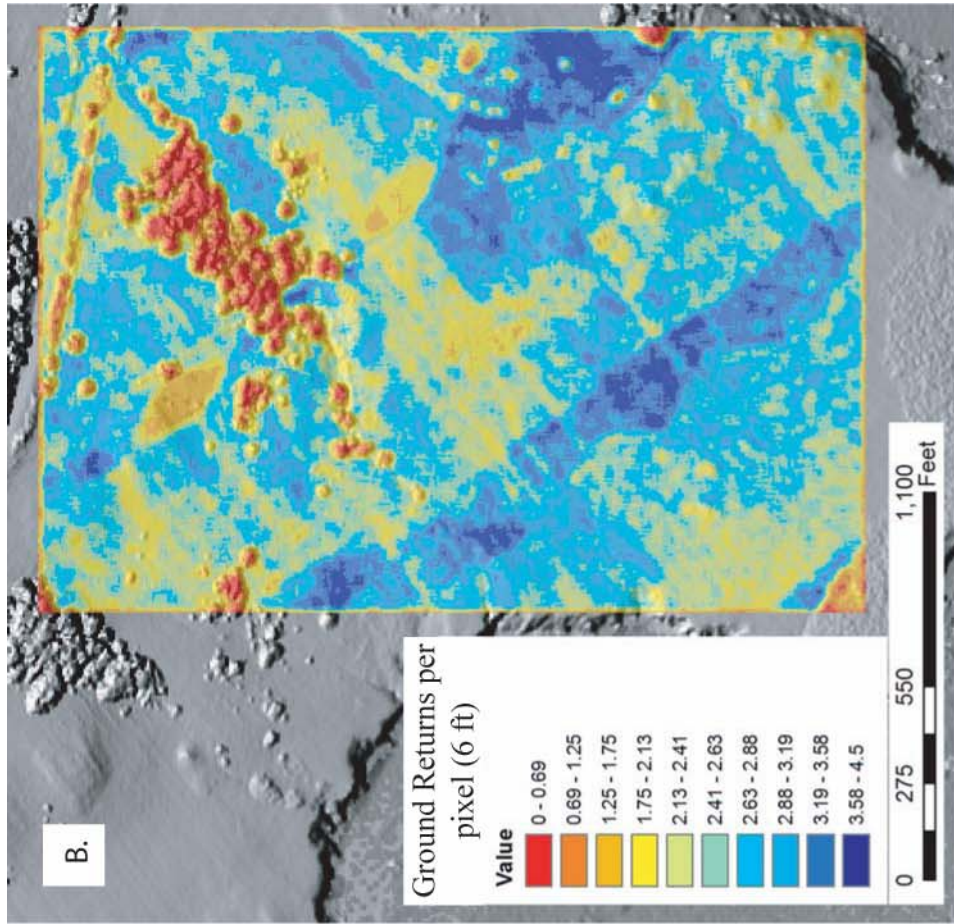
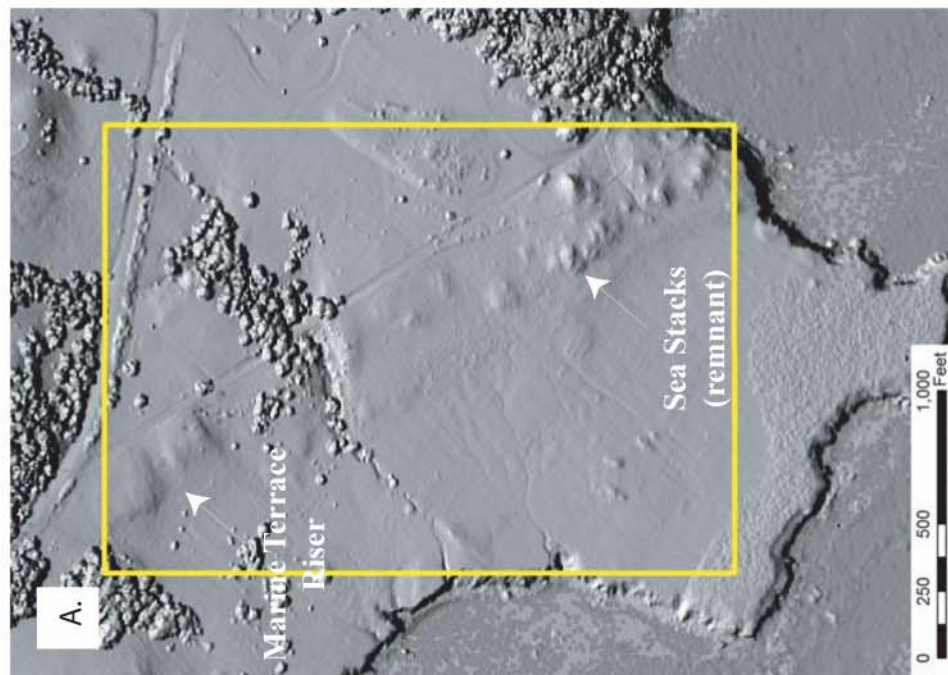


Figure 11. LiDAR return density evaluation. This figure shows the number of LiDAR ground (A) and vegetation (B) returns for each 6 ft pixel in the DEM. Note the limited vegetation returns on the flat, grass-covered, marine terraces and high return density (up to 12 per pixel) in the heavily forested drainages. Also note the very low number of ground returns (< 1 per pixel) beneath the forest canopy (recall Figure I.1C). This lack of ground returns beneath dense vegetation is likely due to poor penetration of the LiDAR pulse through the canopy and the point classification algorithm. The plots show the distribution of points per pixel for both ground (C) and vegetation (D) returns. Note that the majority of 6 ft pixels have 2 or more ground returns. Thus, in certain portions of the data set, it may be appropriate to generate DEMs at resolutions better than 6 ft in order to take full advantage of the richness of these data. Conversely, these figures illustrates that in certain areas, due to poor penetration of the tree canopy, there are very few ground returns. In these areas the density of ground returns may not support the 6 ft DEM resolution as produced by the data vendor. If DEM generation is going to be undertaken in these areas of very low return density, it is necessary to interpolate to span the gaps in the data and thus the method (gridding algorithm) becomes important.



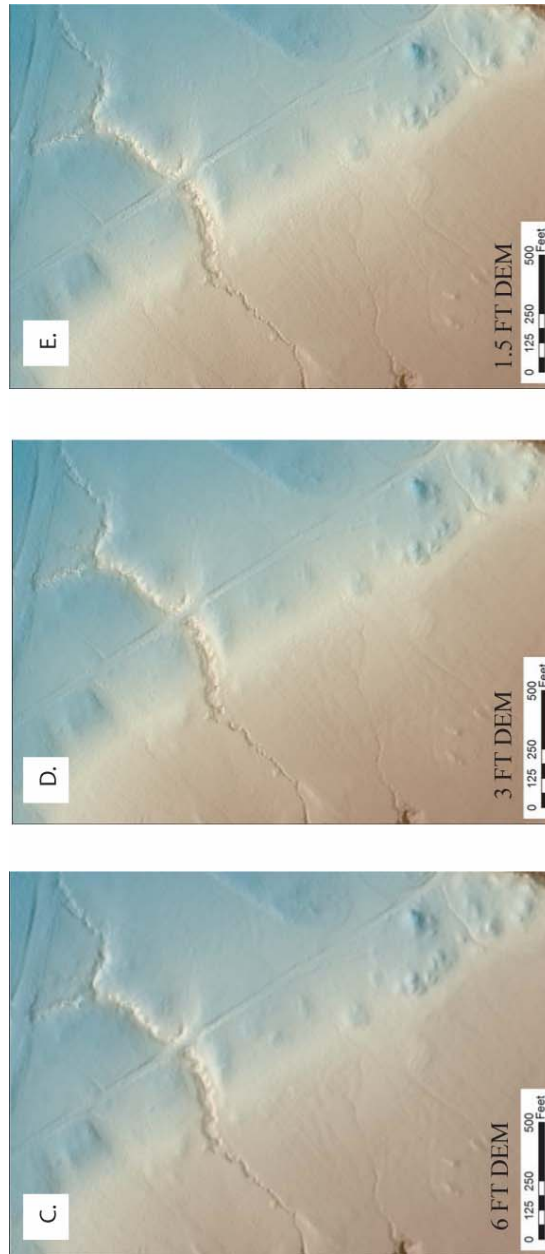


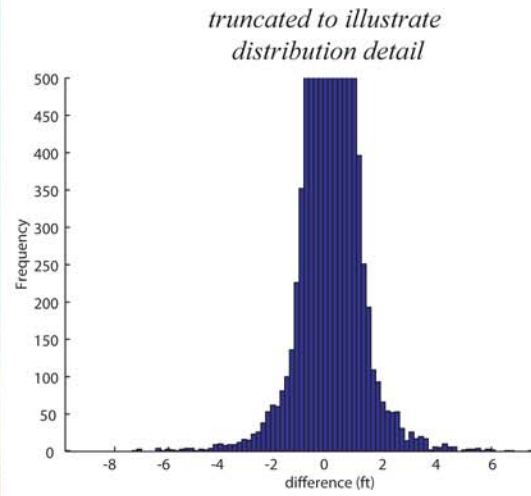
Figure 12. Testing digital elevation model resolution based on LiDAR ground return density. In order to illustrate how and understanding of ground return density can inform the generation of digital elevation models (DEMs) from LiDAR point cloud data, a ~280,000 ground return subset of the Northern San Andreas LiDAR data was selected. A) The dataset extent is shown in the yellow box. This region was selected because it is largely unvegetated and has a high density of ground returns (B). In addition, the area is crossed by a marine terrace riser and also contains a number of sea stack remnants. With the except of the brush in the upper portion of the sample area, the point density evaluation (B) shows that each 6 foot DEM pixel is sampled by at least 2 LiDAR ground returns. This density of ground returns suggests that a DEM at resolutions greater than 6 feet are supported by the data. C) Standard, vendor provided 6 foot DEM for the area shown in (B). D) Point cloud data interpolated to produce a 3 foot DEM. Note the increased clarity of subtle features in the landscape when compared to the 6 ft DEM (C). E) Point cloud data interpolated to produce a 1.5 foot DEM. Again, note the increased clarity of subtle landscape features when compared to both the 6 (C) and 3 foot (D) DEMs. Given the ground return density evaluation shown in (B), the 1.5 foot DEM is likely at the threshold of what is appropriate for this data set.



SPLINE

Mean: 0.025 ft

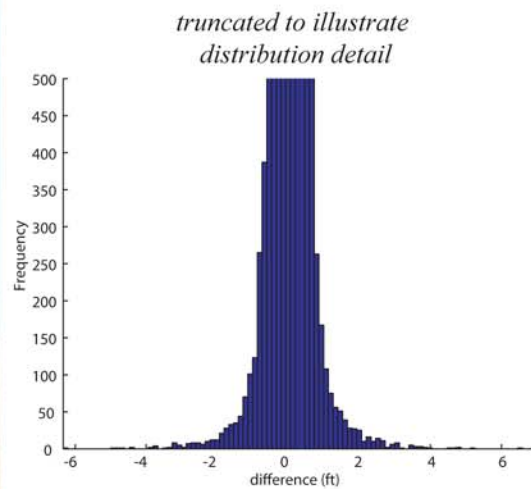
Standard Deviation: 0.27 ft



TIN (Triangular Interpolation Network)

Mean: 0.008 ft

Standard Deviation: 0.16 ft

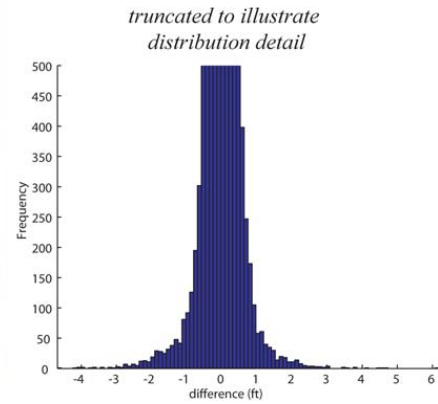




IDW (Inverse Distance Weighted)

Mean: - 0.003 ft

Standard Deviation: 0.15 ft



KRIGING

Mean: - 0.005 ft

Standard Deviation: 0.23 ft

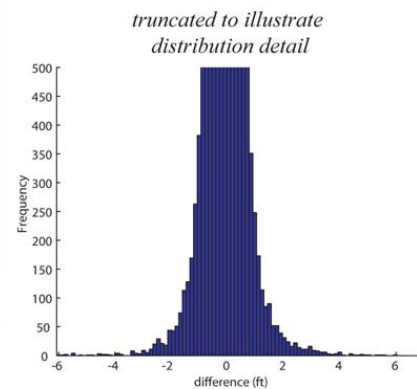
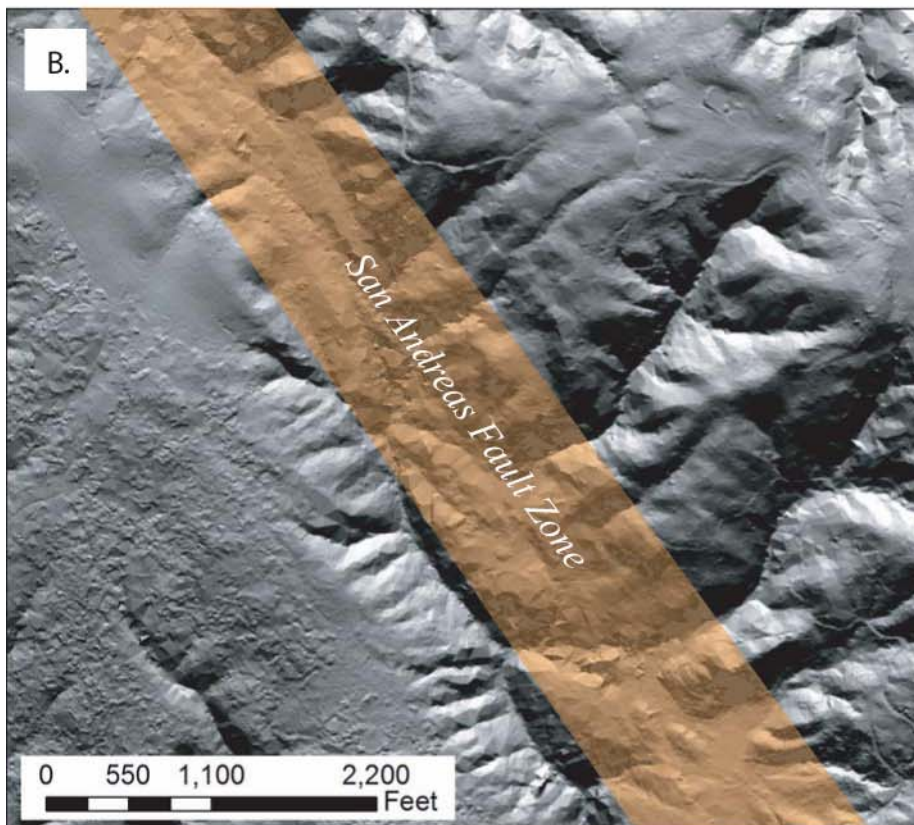
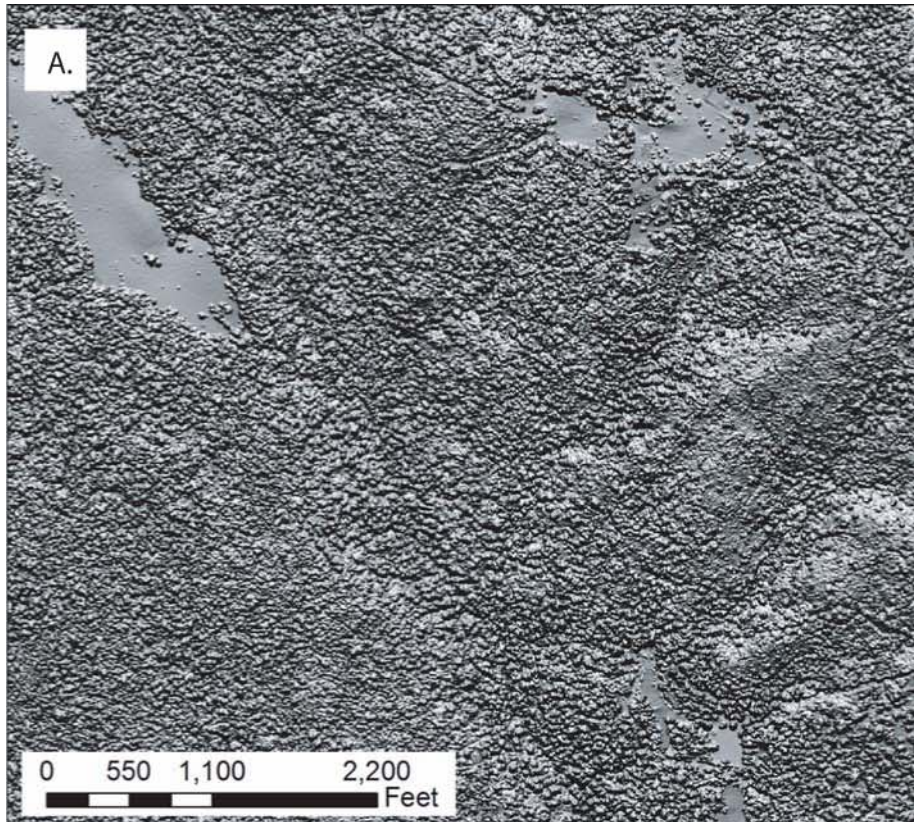
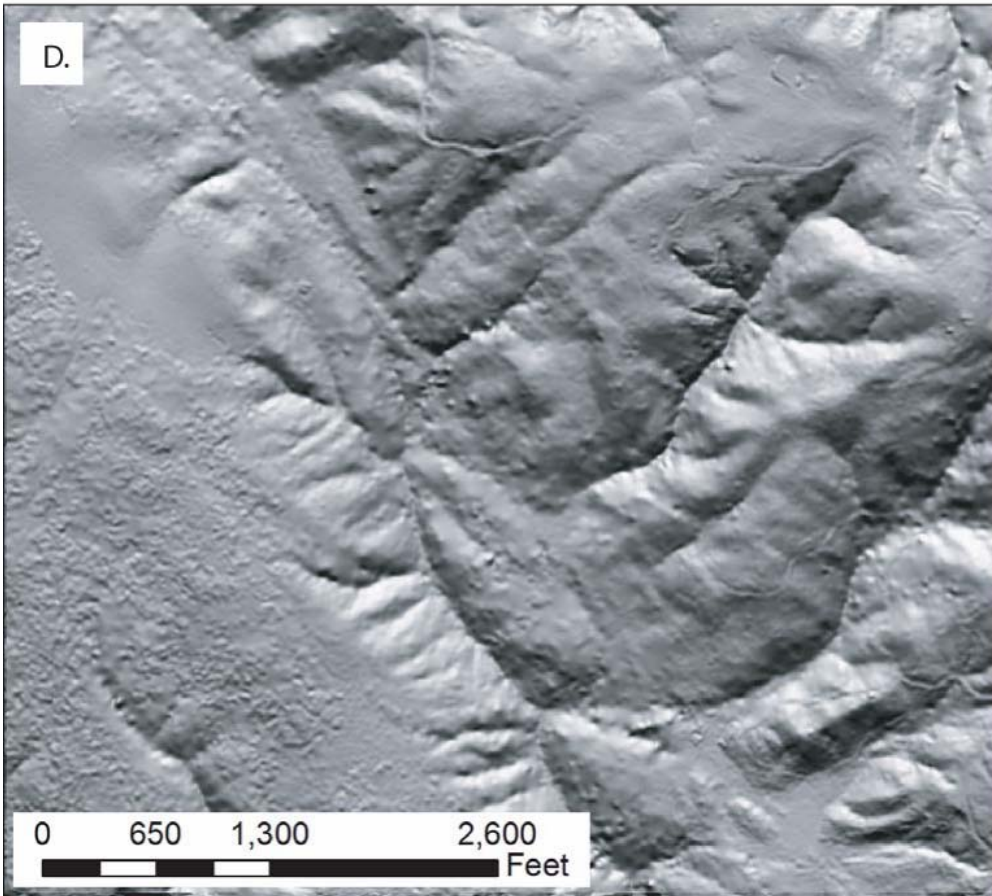
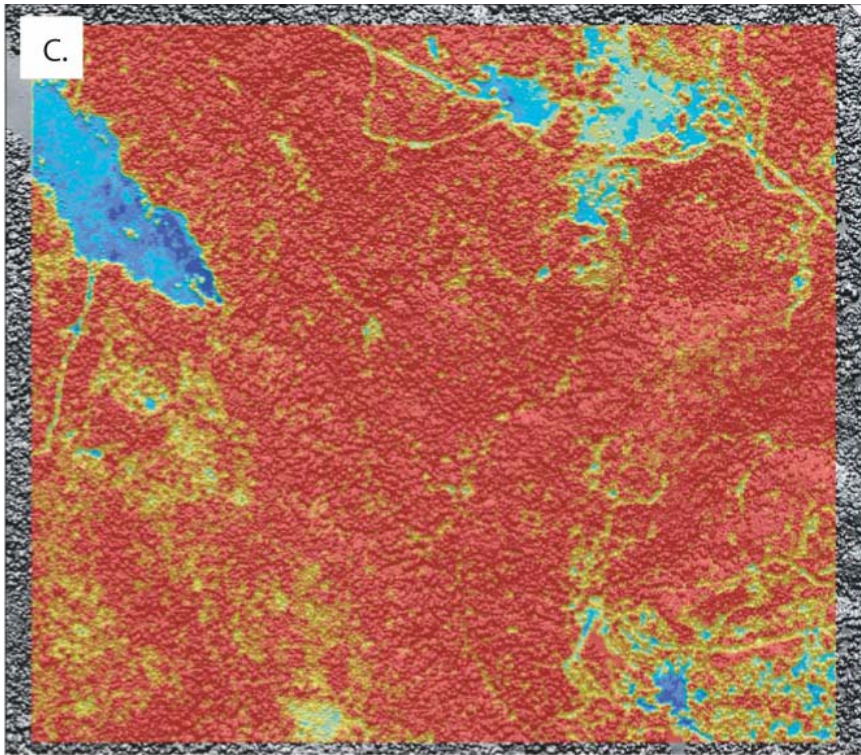


Figure 13. Comparison of common DEM generation interpolation algorithms. The images in this figure explore the accuracy of common DEM interpolation algorithm to fit the LiDAR point cloud. The analysis is performed for the region shown in the yellow box in Figure 12A. Each image is a 3 foot DEM produced with one of four interpolation algorithms: A) Spline B) TIN (Triangular Interpolation Network) C) IDW (Inverse Distance Weighted) D) Kriging. The elevation of the grid at each of the 280,000 individual ground return points was then extracted from the DEMs to test the fit of the surface to the original ground returns. The histograms show the differences between the points and the corresponding DEM pixel. The mean and standard deviation are also indicated. This analysis indicates that in areas of high-ground return density (like this sample data set), there is little variation between interpolation algorithms in the accuracy with which they fit LiDAR ground returns. Therefore, interpolation algorithm is likely not the most important factor in the generation of DEM in such situations.

Figure 14 (following pages). Digital elevation model generation in areas of low ground return density. A) Hillshade of the first return surface (full feature) DEM for a portion of the Northern San Andreas fault (NSAF) LiDAR data (Figure 1) that is characterized by very dense forest canopy on steep slopes. B) Hillshade of the bare earth DEM of the area shown in (A). The San Andreas fault zone crosses the image from the upper left to lower right (with in the orange box). Much of the NSAF is located in landscapes like this example. Although the LiDAR data help to reveal the geomorphology of the SAF fault zone, the density of ground returns in these areas is low due to difficulty of LiDAR penetration through the dense forest canopy. When these data are interpolated, the sparse density of ground returns results in artifacts such as the triangular facets (associated with the TIN interpolation used by the data provider) visible in the bare earth image. Changing interpolation algorithm and/or parameters may enhance the landscape representation in these areas by altering the way that the interpolated surface treats the sparse ground returns. C) This image shows the number of ground returns per 6 foot DEM pixel. Note that in most of the forested areas there is less than one ground return per pixel. Interpolating these data to DEMs of resolutions less than 6 feet would not be appropriate in this case. D) Hillshade of a 6 foot bare earth DEM of the area shown in (A). This DEM was generated by interpolating the same ground return LiDAR point cloud data (~301,000 points) as in (B) but the spline algorithm (settings: DMin=1 ft, tension=40, smoothing=0.1) available in the GEON LiDAR workflow was used instead of a TIN. The spline algorithm does not produce the large facets associated with the TIN so it provides a smoother representation of the landscape. The spline surface is characterized by generally smooth surface with occasional bumps or “pimples”. However, the extent to which the representation of the SAF fault zone geomorphology is enhanced by the spline is open to debate. Furthermore, the triangular facets artifact produced by the TIN are a clear indication of low ground return density. These facets alert the users to the return density problem with the data set while the spline algorithm conceals some of these data density issues and may therefore fool the user into believing that the data set is robust. One could also use a semi-transparent overlay color coded by return density to assess this issue. For the reasons discussed above, users working with these data may wish to further explore the role of interpolation algorithm and parameters in low-ground return environments.





Characterize the tectonic geomorphology of the NSAF at various temporal and spatial scales in order to better understand San Andreas fault geometry, slip distribution and off-fault deformation as manifest in landscape development and response.

In order to address the stated research objectives, we utilized a combination of detailed geomorphic mapping and landform characterization combined with analysis of Digital Elevation Models (DEMs) in a Geographic Information System (GIS) environment. The primary datasets used in this research are late Pleistocene marine terrace mapping (Prentice et al., 2003) and high-resolution digital topography (both 1.8 m and 10 m DEMs) from LiDAR and the USGS National Elevation Dataset (NED).

Prentice (1989) provides a late Pleistocene slip rate for the SAF at Alder Creek of 16 to 24 mm/yr based on tentative terrace correlations (Muhs et al., 2003; Prentice et al., 2000 and 2001). This slip rate is the only Pleistocene rate for the SAF north of Point Reyes and is a critical data point for understanding SAF system behavior and segmentation. This slip rate is based upon the terrace mapping shown at left. The uncertainty in terrace correlation translates directly into uncertainty in the late Pleistocene slip rate for the SAF at Alder Creek. One of the greatest areas of uncertainty in the terrace correlation is matching the terraces across the SAF. The significant elevation difference of the terraces across the SAF raises questions about the validity of the correlation.

Figure 15 shows our tentative correlation for the three lowest, late Pleistocene, marine terraces between Fort Ross and Mendocino overlain on a hillshade of the Northern San Andreas fault LiDAR dataset. This terrace correlation was established via geomorphic mapping from aerial photography and LiDAR data and with simple relative position arguments. This terrace correlation provides an important datum that may be used to constrain horizontal and vertical deformation associated with the SAF. Age control for the late Pleistocene terraces along this portion of coastal California is limited to three Alpha-spectrometric U-series analysis of three marine terrace corals collected near the Point Arena Lighthouse (Muhs et al., 1990, 1994, 2003).

We have compiled an updated map of the late Pleistocene marine terraces along approximately 125 km of coastline in Sonoma and Mendocino Counties. To determine the elevation of the marine terrace inner edges throughout the study area, we began with the inner edge mapping shown in Figure 15. Next, the elevations of the inner edges were extracted from the NSAF LiDAR DEM. Analysis of this mapping in tandem with the NSAF LiDAR data suggests significantly higher marine terrace elevations in an area bounded by the SAF on the south and the Navarro River to the north. Figure 16 shows the inner edge elevations of the three lowest marine terraces between Fort Ross and Mendocino. These terraces provide an excellent marker for the study of spatial and temporal variation in off-SAF deformation. The plot shows elevation vs. the northing component of the California State Plane coordinate system.

If uplift rates north of the SAF are in fact higher, this signal should also be expressed in older portions of the landscape. To test this hypothesis, we undertook an analysis of local relief in the high topography adjacent to the marine terraces (Figure 17). 10 m DEMs were used to construct topographic envelopes and sub-envelopes and to calculate the topographic residual (e.g. Burgmann et al., 1994). Through the analysis of envelope/sub-envelope residuals, zones of high relief can be located in the landscape. These zones have been shown to correspond directly with regions of greatest tectonic uplift and deformation. The topographic residual analysis provides an independent test of the apparent differential uplift observed in the marine terraces and may be an opportunity to constrain SAF fault geometry and/or segmentation.

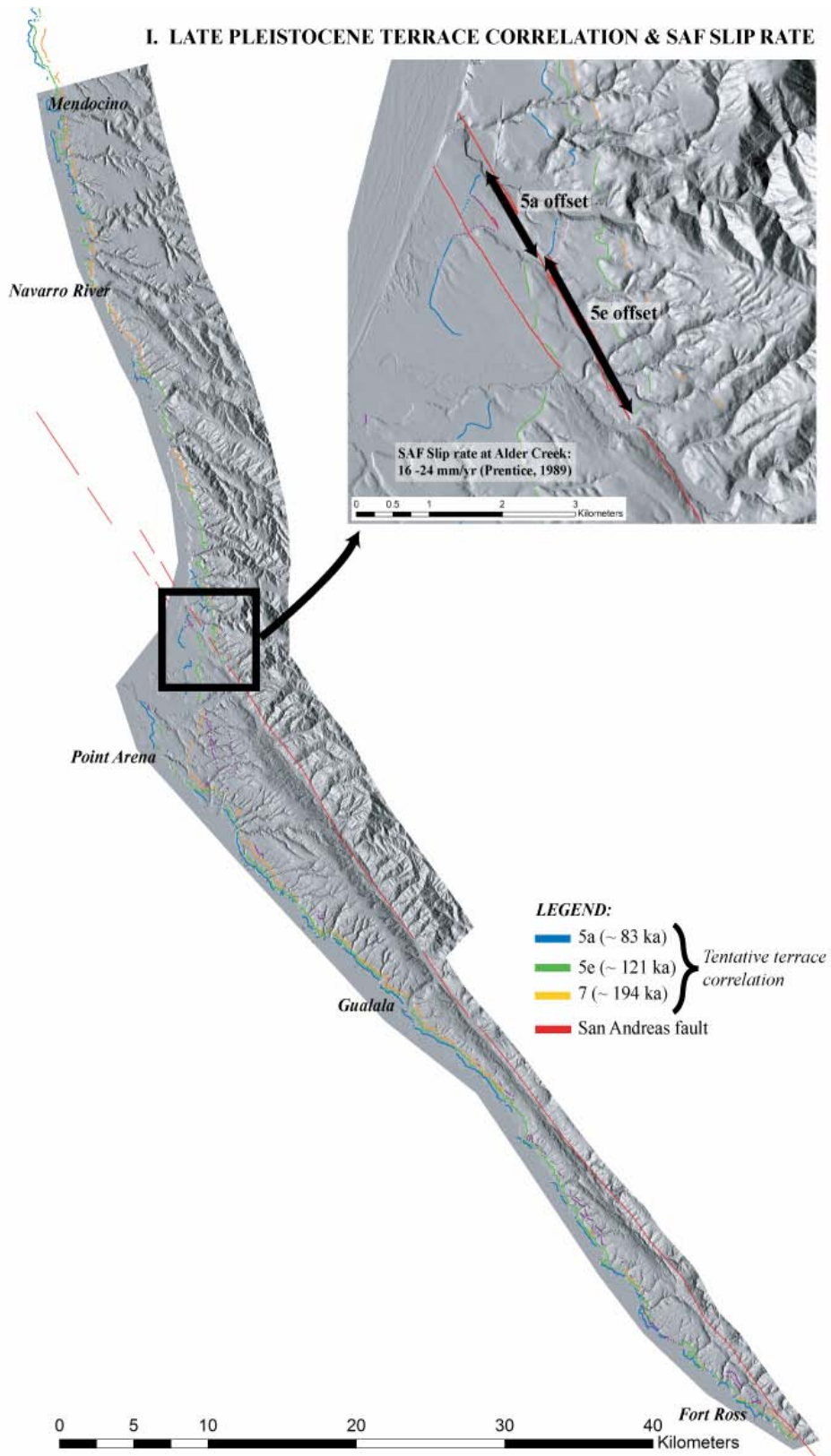
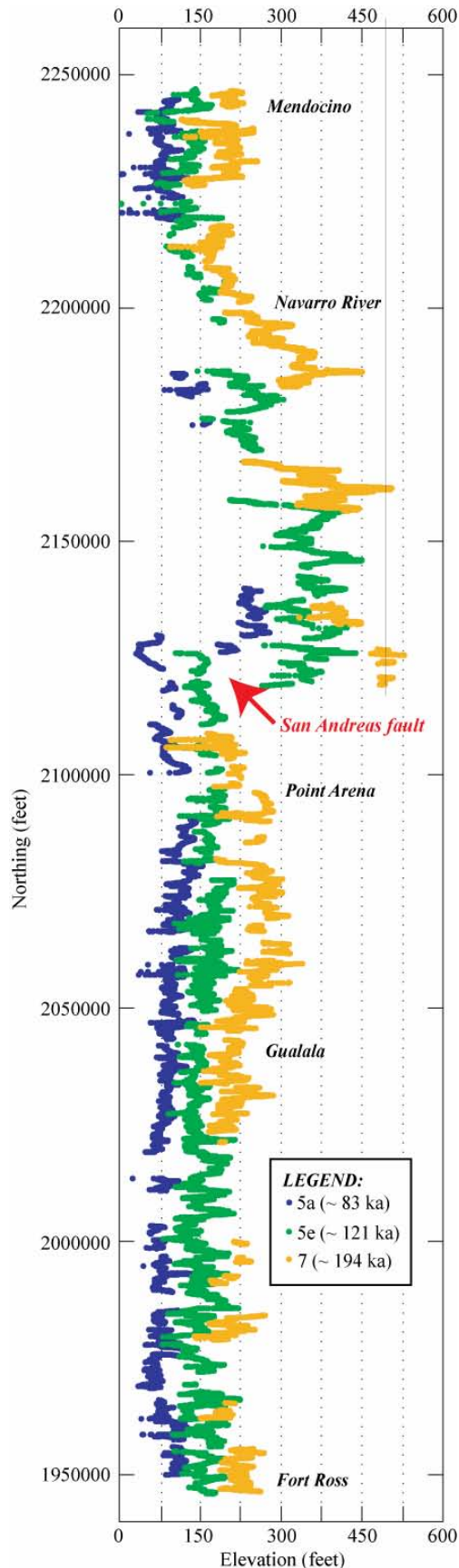


Figure 15. Overview of NSAF LiDAR with mapping of the San Andreas Fault and marine terraces. See text for explanation.



Commentary about terrace elevation plot (figure 16):

- Inner edge elevations for the three lowest marine terraces are significantly higher immediately to the north of the SAF than they are at greater distances north or south of the SAF.
- The area of elevated marine terraces is bound by the SAF on the south and the Navarro River to the north. This bulge in the terraces is asymmetric with the highest elevations immediately to the north of the SAF. Terrace elevations decreasing gradually to the north until they level off just north of the Navarro.
- Terrace elevations at the southern and northern ends of the study area are similar.
- Warping of the terraces between Gualala and Point Arena may indicate increased uplift rates in this area as well.
- The scatter in elevations for a given terrace inner edge is largely due to variation in the thickness of sediment / colluvium overlying the bedrock terrace platform. Other factors contributing to the elevation scatter include digitizing errors and locations where the inner edge mapping crosses drainages incised into the terrace.
- Plots such as this one provide an indication of potential errors in the terrace correlation and should help to guide us to refine the terrace mapping and correlation

Assuming the terrace correlation is correct, tentative late Pleistocene uplift rates vary by a factor of three in the study area:

- Immediately north of the SAF: ~0.75 - 0.95 mm/yr
- South of Gualala/near Mendocino: ~0.28 - 0.38 mm/yr

Figure 16. Marine terrace inner edge elevations versus distance along the coast in feet. Variable elevations indicate differential surface uplift along the coast.

The greatest local topographic relief is immediately north of the SAF. This zone of high relief extends northward to the Navarro and east to the edge of the study area. Intuitively, the area of greatest local relief corresponds directly with the area of highest topography in the study area. The geometry of the high relief region suggests uplift adjacent to the SAF and tilting of the range up and away from the fault. The hinge for this tilting appears to be just to the north of the Navarro. The orientation of the Navarro is almost perfectly coincident with the margin of the high relief zone, one may hypothesize that the location of the Navarro has been migrating northward with time as the topography to the south gains elevation, forcing the drainage to slip to the north. The spatial correlation between high topographic residuals and increased terrace elevations suggests that the observation of elevated inner edge elevations are due to higher uplift rates north of the SAF and not due to errors in the marine terrace correlation.

In summary, it is possible to infer that the 16-24 mm/yr slip rate given by Prentice (1989) for the SAF at Alder Creek is valid. Assuming the terrace correlation is correct, uplift rates just north of the SAF are ~0.75 - 0.95 mm/yr. Rates away from the SAF in the study area are approximately three times slower at ~0.28 - 0.38 mm/yr. Additional work is necessary to examine possible Pliocene marine terrace units (e.g. Higgins, 1960) in the higher topography that may be used to constrain vertical deformation rates over a longer temporal range. Boundary element modeling of the observed deformation pattern can be used to help to constrain SAF geometry.

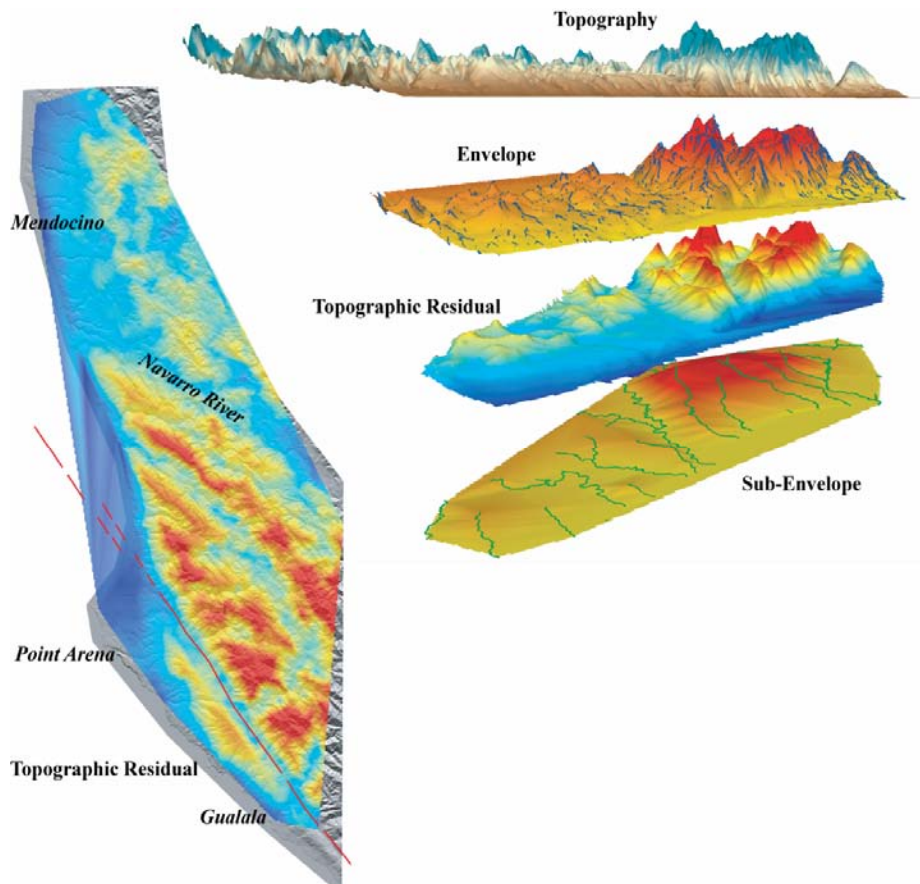


Figure 17. (top to bottom on right): current topography in the study area, envelope surface and points used to construct it, topographic residual and sub-envelope with channels that constrain this surface. On the left is the topographic residual shown in map view. Note that the areas of greatest local relief are located north of the SAF and south of the Navarro River.

Presentations and Publications

Thesis: Christopher Crosby, M. S., A geoinformatics approach to LiDAR data distribution and processing with applications to geomorphology, Arizona State University, August, 2006.

Crosby, C.J., Prentice, C.S., Merritts, D., Gardner, T., in preparation, Digital database of marine terrace mapping and correlation, Fort Ross to Mendocino: coastal northern California.

Crosby, C. J., Arrowsmith, J R., Prentice, C. S., Application of LiDAR data to constraining a late Pleistocene slip rate and vertical deformation of the Northern San Andreas Fault, Fort Ross to Mendocino, California: Collaborative research between Arizona State University and the U.S. Geological Survey, *in* 4th Annual Northern California Earthquake Hazards Workshop abstract volume, Menlo Park, CA, January 18-19, 2007.

Crosby, C. J., Arrowsmith, J R., Prentice, C. S., Application of LiDAR data to constraining a late Pleistocene slip rate and vertical deformation of the Northern San Andreas Fault, Fort Ross to Mendocino, California: Collaborative research between Arizona State University and the U.S. Geological Survey, *in* 3rd Annual Northern California Earthquake Hazards Workshop abstract volume, Menlo Park, CA, January 18-19, 2006.

Arrowsmith, J R. and Crosby, C.J., New Looks at Active Faults: Tectonic Geomorphology using Airborne Laser Swath Mapping (ALSM), Presented at the 100th Anniversary Earthquake Conference (SSA), San Francisco, CA April 18-21, 2006.

Crosby, C.J. and Arrowsmith, J R., Utilization of LiDAR / ALSM Point Cloud Data for Earthquake Geology and Tectonic Geomorphic Mapping, Analysis, and Visualization, Presented at the 100th Anniversary Earthquake Conference, San Francisco, CA April 18-21, 2006.

Crosby, C. J., Arrowsmith, J R., Oldow, J. S., Prentice, C. S., Exploiting LiDAR for Regional Morphologic Correlation and Dating of Wave-cut and Fault-Controlled Landforms, *Eos Trans. AGU*, (47), Fall Meet. Suppl., Abstract G13B-0810, 2004.

References (not cited above as products of this research)

- Hanks, T.C., 2000, The Age of Scarplike Landforms From Diffusion-Equation Analysis, *In* Noeller, J.S., Sowers, J.M., Lettis, W.R. eds., *Quaternary Geochronology: Methods and Applications*: American Geophysical Union, Washington, D.C., 582 p.
- Hanks, T.C., Bucknam, R.C., Lajoie, K.R., Wallace, R.E., 1984, Modification of Wave Cut and Faulting-Controlled Landforms: *Journal of Geophysical Research*, v. 89, p. 5771-5790.
- Hanks, T.C., Wallace, R.E., 1985, Morphological Analysis of the Lake Lahontan Shoreline and Beachfront Fault Scarps, Pershing County, Nevada: *Bulletin of the Seismological Society of America*, v. 75, p. 835-846.
- Hilley, G. E., 2001, Landscape development of tectonically active areas: Tempe, Arizona, Arizona State University, Ph.D. dissertation.
- Hilley, G.E., and Arrowsmith, J.R., 2001, Transport and production-limited fault scarp simulation software, in: Merritts, D., Burgman, R., *Tectonics and Topography: Crustal Deformation, Surface Processes, and Landforms: Geological Society of America Short Course Manual*, 66 p.
- Jennings, C.W., 1994, Fault activity map of California and adjacent areas, with locations and ages of recent volcanic eruptions: California Division of Mines and Geology, Geologic Data Map No. 6, map scale 1:750,000.
- Muhs, D.R., Prentice, C.S., and Merritts, D.J., 2003, Marine terraces, sea level history and Quaternary tectonics of the San Andreas fault on the coast of California, in: Easterbrook, D.J., editor, *Quaternary Geology of the United States, INQUA 2003 Field Guide Volume*, Desert Research Institute, Reno, NV, p. 1-18.
- Muhs, D.R., Kennedy, G.L., Rockwell, T.K., 1994, Uranium-series ages of marine terrace corals from the Pacific coast of North America and implications for last interglacial sea level history: *Quaternary Research*, v. 42, p. 72-87.
- Muhs, D.R., Kelsey, H.M., Miller, G.H., Kennedy, G.L., Whelan, J.F., and McNelly, G.W., 1990, Age estimates and uplift rates for late Pleistocene marine terraces: Southern Oregon portion of the Cascadia forearc: *Journal of Geophysical Research*, v. 95, p. 6685-6698.
- Prentice, C.S., Crosby, C.J., Harding D.J., Haugerud, R.A., Merritts, D.J., Gardner, T., Koehler R.D., Baldwin, J.N., 2003, Northern California LIDAR Data: A Tool for Mapping the San Andreas Fault and Pleistocene Marine Terraces in Heavily Vegetated Terrain [abs.]: *EOS, Transactions of the American Geophysical Union*, v. 84(46), Abstract G12A-06.
- Paleoseismic and Quaternary tectonic studies of the San Andreas Fault between Shelter Cove and Fort Ross, Northern California, USA [abs.]: *Ten Years of Paleoseismology in the ILP: Progress and Prospects*, 17-21 December, 2001, Kaikoura, New Zealand, Programme and Abstracts. Institute of Geological and Nuclear Sciences Information Series 50, p. 52-53.
- Prentice, C. S., Prescott, W.H., Langridge, R., And Dawson, T., 2001, New geologic and geodetic slip rate estimates on the North Coast San Andreas Fault: approaching agreement? [abs.]: *Seismological Research Letters*, v. 72, P. 282.
- Prentice, C.S., Langridge, R., and Merritts, D.J., 2000, Paleoseismic and Quaternary tectonic studies of the San Andreas fault from Shelter Cove to Fort Ross, *In: Proceedings of the 3rd conference on Tectonic Problems of the San Andreas Fault System*, Bokelman, G., and Kovach, R.L., Eds., Stanford University, Stanford, California.
- Prentice, C.S., 1989, Earthquake geology of the northern San Andreas fault near Point Arena, California: Pasadena, California, California Institute of Technology, Ph.D Dissertation, 252 p.
- Rosenbloom, N.A. and Anderson, R.S., 1994, Hillslope and channel evolution in a marine terraced landscape, Santa Cruz, California: *Journal of Geophysical Research*, v.99, p. 14013-14029.